
Article:
Liu, L. orcid.org/0000-0002-1103-7445, Zhang, J. orcid.org/0000-0001-9638-574X, Feng, Z. et al. (3 more authors) (2025) Contactless and Continuous Blood Pressure Detection with FMCW Millimeter-Wave Radar. IEEE Sensors Journal. ISSN 1530-437X

https://doi.org/10.1109/jsen.2025.3548259

Contactless and Continuous Blood Pressure Detection with FMCW Millimeter-Wave Radar

Luyao Liu, *Graduate Student Member, IEEE*, Jie Zhang, *Member, IEEE*, Ziyang Feng, Sen Zhang, Zhiqiang Zhang, *Member, IEEE*, and Wendong Xiao, *Senior Member, IEEE*

***Abstract*— Blood pressure (BP) is a vital sign that could provide crucial information for the prevention, diagnosis and treatment of many diseases. Most of the existing BP detection solutions require physical contact between human skin and sensor, which may be frustrated due to uncomfortable experience and extra burden. Recently, millimeter-wave (mm-wave) radar based BP detection has attracted more attention, but it is confronted with the challenges on noise interference, fine-grained arterial pulse signal recovery and shortage of annotated samples for training BP estimation model. In this paper, we develop mmRBP, a contactless and continuous BP detection system with a single frequency modulated continuous wave (FMCW) mm-wave radar. mmRBP consists of three modules. The arterial pulse motion extraction module is designed to mitigate the noise interference, in which the range fast Fourier transform (range-FFT) and digital beamforming (DBF) are applied to scan the space and the direction with the strongest arterial pulse motion is identified. Then, the arterial pulse signal translation module is devised to transform the mm-wave reflections to fine-grained arterial pulse signal by the convolutional neural network (CNN) based translation filter. Finally, the BP estimation module is designed to address the issue of shortage of annotated radar training samples, where a deep transfer learning (DTL) model is employed to transfer the knowledge of the source network trained by the public BP dataset to the target network trained by the collected radar dataset. Results of extensive experiments show that the error of mmRBP is 0.87±6.12 mmHg (Mean error±Standard Deviation) and 0.59±3.78 mmHg for systolic BP (SBP) and diastolic BP (DBP), which satisfy both the British Hypertension Society (BHS) and the Association for the Advancement of Medical Instrumentation (AAMI) BP measurement standards.**

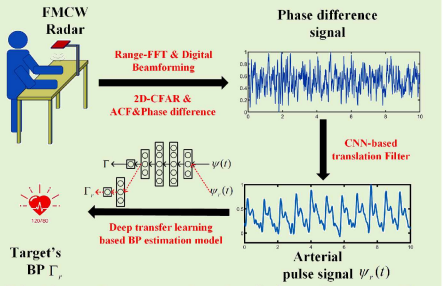

***Index Terms*— Blood pressure, mm-wave radar, contactless detection, deep transfer learning.**

I. Introduction

This work was supported in part by the National Natural Science Foundation of China (NSFC) under Grant 62173032 and Grant 62003038, the Foshan Science and Technology Innovation Special Project under Grant BK22BF005, the Regional Joint Fund of the Guangdong Basic and Applied Basic Research Fund under Grant 2022A1515140109, the Fundamental Research Funds for the Central Universities under Grant FRF-TP-22-014A1, and the Natural Science Foundation of Shandong Province under grant ZR202212040125. (Corresponding author: Wendong Xiao.)

Luyao Liu, Ziyang Feng, Sen Zhang and Wendong Xiao are with the School of Automation and Electrical Engineering, University of Science and Technology Beijing, Beijing 100083, China. (e-mail: b20180299@xs.ustb.edu.cn; fengziyang13@126.com; zhangsen@ustb.edu.cn; wdxiao@ustb.edu.cn). Wendong Xiao is also with the Beijing Engineering Research Center of Industrial Spectrum Imaging, Beijing 100083, China, and with the Shunde Innovation School, University of Science and Technology Beijing, Foshan 528399, China.

Jie Zhang is with the Centre for Wireless Innovation, Queen's University Belfast, BT3 9DT Belfast, U.K. (e-mail: jie.zhang@qub.ac.uk).

Zhiqiang Zhang are with the School of Electronic and Electrical Engineering, University of Leeds, LS2 9JT Leeds, U.K. (e-mail: z.zhang3@leeds.ac.uk).

This work was conducted in accordance with the principles of the Declaration of Helsinki and in full compliance with statutory requirements of China. Ethical approval for the radar-based blood pressure detection research was obtained from the Review Board of University of Science and Technology Beijing, with approval reference number 2024-4-1. We confirm that written informed consent was obtained from all participants, and the study was conducted in accordance with ethical guidelines.

BLOOD pressure (BP) is one of the vital signs that refers to the lateral pressure of blood per unit area against the aortic wall [1]. BP varies between systolic BP (SBP) and diastolic BP (DBP), embodying rich information about health status of the human subject [2], [3]. Hypertension is a risk factor for many diseases, such as arrhythmia, heart attack, blindness, and brain stroke [4], [5]. It is estimated that there are 1.13 billion people worldwide who suffer from hypertension [6]. However, most patients are unaware that they have hypertension until a cardiovascular event occurs, which could be avoided by continuous BP detection in the daily life.

In the past decades, a variety of BP detection solutions have been developed. The traditional solutions are to place particular medical devices to the arterial line of the human subject [7]. Although the solution is regarded as "gold standard", it is invasive and may cause pain or risk of infection. Non-invasive BP detection has been advocated as a promising alternative due to its safety and convenience. Most of existing non-invasive BP detection solutions require cuffs or other wearable sensors to be in contact tightly with human skin during BP detection [8]–[11], which may cause extra burden and uncomfortable experience, especially for those special patients who suffer from skin allergy and burn. To achieve BP detection in a contactless manner, camera-based solutions [12]–[16] and radio frequency (RF) based solutions [17]–

[22] have been proposed. Camera-based solutions exploit the property of video/image data caused by arterial pulse motion to estimate BP [12]. However, they are sensitive to the lighting conditions and might cause severe privacy concerns, which are further limited in the practical deployment. Differently, RF-based sensing does not depend on lighting conditions, and can bring better privacy protection. It has attracted more attention in numerous applications, such as vital sign detection [23]–[25], seismocardiogram and electrocardiogram recovery [26], [27], heart sound detection [28]. RF-based solutions leverage on the variations of RF signals caused by arterial pulse transmission to estimate BP [29]. Among them, mm-wave radar has demonstrated its promising potential due to its high frequency and wide bandwidth [30], [31].

In recent years, many efforts have been focused on radar-based BP detection, leveraging the pulse wave velocity (PWV). The relationship between BP and PWV has been studied extensively, ultimately revealing that PWV is proportional to BP [32], [33]. PWV is measured by the pulse transit time (PTT) between two nodes in different parts of the body. Some attempts employed radar in conjunction with wearable ECG or PPG sensors to obtain PTT and infer BP [34]–[36]. Buxi *et al.* [35] applied 1.1 GHz continuous wave (CW) radar in the neck/chest and impedance echocardiography sensors in the waist/shoulder to measure the PTT and pulse arrival times (PATs), which were calibrated to the SBP and DBP via the linear regression. However, these attempts may cause discomfort and are not applicable to patients with skin diseases or burns due to the usage of the contact sensors. Subsequently, some solutions attempted to employ multiple radars to calculate PTT for inferring BP [37]–[39]. In [38], a dual-frequency radar system was designed to detect the PTT and PWV for BP estimation, which includes a 5.8 GHz single-antenna radar for chest movement detection and a 120 GHz miniaturized radar for pulse detection. Although these solutions only use radar, they are far from practical as a strict synchronization between the multiple sensors are needed, while those tricky placements can be very unrealistic to achieve in the daily environment. Moreover, PWV-based BP detection requires a calibration, making it less robust regarding generalization ability.

Motivated by the above observations, we propose a novel BP detection system, mmRBP, leveraging a single FMCW mm-wave radar, which acquires the fine-grained pulse wave signal and relies on the machine learning algorithm to estimate BP, by skipping the explicit PTT calculation and calibration as done in previous works. However, it is not a trivial task and several fundamental challenges remain to be addressed. First, it is challenging to extract mm-wave reflections containing arterial pulse motion due to the noise interference from the body and the environment. In practice, the mm-wave reflections corresponding to arterial pulse motion are weak and usually buried under the interference and background noise from the environment. Most of the existing approaches selected the bin with the maximum energy in the range-azimuth plane to extract the phase signal [17], [40], [41]. Unfortunately, it might not perform well especially when the wrist is not facing the radar. This is because the direction of the strongest reflection may not coincide with the arterial pulse motion but rather a different location on the arm. As a result, the signal-to-noise ratio (SNR) of extracted phase signal may be low.

Second, it is challenging to acquire the fine-grained arterial pulse signal from the mm-wave reflections. Most of the existing approaches applied the traditional filters [41], [42] or signal decomposition approaches [40] to extract arterial pulse signal. However, these approaches may filter out some useful detailed information in the arterial pulse signal, such as dicrotic waves, dicrotic north and so on, which makes it difficult to extract pulse-related features effectively for BP estimation.

Third, it is challenging to establish the BP estimation model with small amount of training samples. The diverse features were extracted from pulse signal to calculate BP based on the machine learning algorithms, including pulse amplitude, area under the curve (AUC), width, peak, derivatives, and various delays [17], [43], [44]. Jung *et al.* [45] extracted the characteristics of heart sounds and certain features in the time and frequency domains from the radar pulse signal, and employed support vector machine (SVM) to estimate BP. In [41], the multiple related features were extracted from radar pulse signals and a random forest based BP regression model was established. However, when the mm-wave reflections are contaminated by noise, it is difficult to extract effective features from coarse-grained radar pulse signal. Furthermore, deep learning techniques automatically extracted features through neural networks to estimate BP. Ran *et al.* [20] designed an encorder-decorder neural network to derive the cardiovascular information from the extracted radar signal to estimate BP. A transformer network based BP estimation model was proposed to achieve radar-based BP detection, which includes convolutional layers with different scales, a gated recurrent unit (GRU) and multi-head attention modules [40]. However, it is crucial for machine learning based BP estimation approaches to collect a large amount of training samples, which brings a heavy obstacle for most of the existing radar-based BP detection approaches.

In this paper, to tackle the aforementioned challenges, the proposed mmRBP consists of three key functional modules. In the arterial pulse motion extraction module, the range fast Fourier transform (range-FFT) and digital beamforming (DBF) divide the space into different range-azimuth bins and the bin with the strongest arterial pulse motion (also known as arterial pulse bin) is identified to extract phase signal with high SNR. In the arterial pulse signal translation module, the extracted phase signal is translated to fine-grained arterial pulse signal by convolutional neural network (CNN) based translation filter. In the BP estimation module, a deep transfer learning (DTL) based BP estimation model is designed. The source network of DTL consists of several CNN blocks, a bidirectional GRU (Bi-GRU) block, a self-attention (SA) block and three full connected (FC) layers, which is trained using the public BP dataset. The parameters of the first several layers in the source network are transferred to the corresponding layers of the target network, then the parameters of remaining layers are fine-tuned using the radar samples. We implement mmRBP using a commercial off-the-shelf mm-wave radar and perform extensive experiments to validate the performance of mmRBP.

The experimental results satisfy both the British Hypertension Society (BHS) and the Association for the Advancement of Medical Instrumentation (AAMI) BP measurement standards.

Our major contributions are summarized as follows:

1) We develop a novel BP detection system, mmRBP, leveraging a single FMCW mm-wave radar, which enables accurate and continuous BP detection in a contactless manner.
2) We design an arterial pulse motion extraction module to extract mm-wave reflections with high SNR by range-FFT, DBF and arterial pulse bin identification, and an arterial pulse signal translation module to recover fine-grained arterial pulse signal by CNN-based translation filter. These two modules effectively mitigate noise interference and extract high-quality arterial pulse signal.
3) We design a DTL-based BP estimation model, in which the parameters of a pre-trained source network can be reused, and the only last few layers in the target network need to be trained with a small amount of radar samples. Hence, the model reduces the amount of radar samples and computational cost, potentially enabling the real-world deployment.

The rest of this paper is organized as follows. The proposed mmRBP is presented in detail in Section II. Experimental performance is evaluated in Section III. The conclusions are given in Section IV.

II. System Design

As illustrated in Fig. 1, mmRBP emits electromagnetic wave (EM) signals at the wrist and captures reflected signals. By processing the reflected signal, mmRBP could achieve BP detection, which is mainly composed of three modules: arterial pulse motion extraction module, arterial pulse signal translation module and BP estimation module. First of all, mmRBP divides the space to different range-azimuth bins by range-FFT and DBF, and focus on the arterial pulse bin. Then, the extracted phase difference signal in the arterial pulse bin is translated to fine-grained arterial pulse signal with the help of CNN-based translation filter. Finally, the BP can be obtained from the arterial pulse signal by transfer learning algorithm.

A. Signal Model

mmRBP is built on a FMCW mm-wave radar, which transmits a series of waveforms named chirp signals. The instantaneous frequency of the chirp signal increases linearly as time, as shown in Fig. 2, and can be written as

$$f(t) = f_{min} + \frac{B}{T_d}t, \tag{1}$$

where f_{min} is the chirp starting frequency, T_d is the chirp duration and B is the bandwidth. The transmitted chirp signal $x_T(t)$ can be written as

$$\begin{aligned} x_T(t) &= A_T \cos\left(2\pi \int_0^t f(\tau)d\tau + \varphi(t)\right) \\ &= A_T \cos\left(2\pi f_{min} + \pi \frac{B}{T_d}t^2 + \varphi(t)\right), \end{aligned} \tag{2}$$

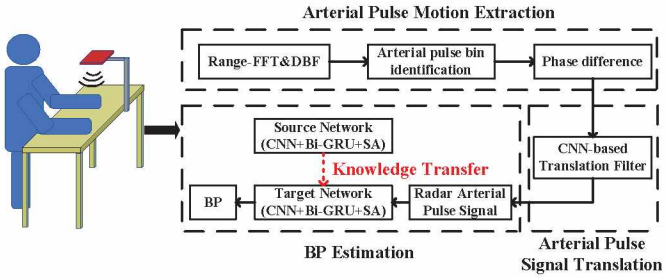

Fig. 1. Processing flow of mmRBP

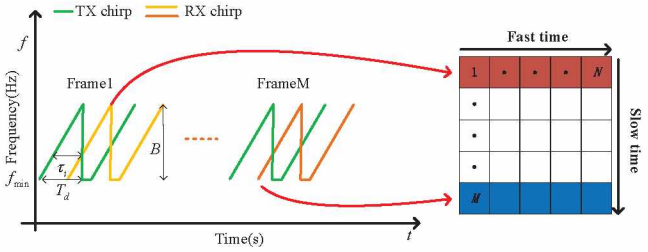

Fig. 2. FMCW radar signal

where A_T is the amplitude of the transmitted signal, φ is the phase noise. The received signal $x_R(t)$ can be denoted as

$$\begin{aligned} x_R(t) = A_R \sum_{i=1}^{\Omega} \cos\Big[&2\pi f_{\min}(t-\tau_i) + \pi \frac{B}{T_d}(t-\tau_i)^2 \\ &+\varphi(t-\tau_i)\Big], \end{aligned} \tag{3}$$

where A_R is the amplitude of the received signal, τ_i denotes the round-trip delay caused by the subject in the i-th reflection path, which can be expressed as $\tau_i = \frac{2d_i(t)}{c}$, where c is the speed of light, $d_i(t)$ is the range between the subject and radar, Ω is the number of reflection points in the environment.

The received signal is mixed with a replica of the transmitted signal, and then the high-frequency components of the mixed signal are filtered out to obtain the intermediate frequency (IF) signal $x_{IF}(t)$:

$$\begin{aligned} x_{IF}(t) = A \sum_{i=1}^{\Omega} \cos\Big[&2\pi \frac{B\tau_i}{T_d}t + 2\pi f_{\min}\tau_i - \pi \frac{B}{T_d}{\tau_i}^2 \\ &+\Delta\varphi(t)\Big], \end{aligned} \tag{4}$$

where A is the amplitude of the IF signal. The residual phase noise $\Delta\varphi(t)$ can be neglected for short range scenarios, and the term $\pi\frac{B}{T_d}{\tau_i}^2$ can be also ignored as it is very small. The complex IF signal can be obtained by two orthogonal I/Q channels, which is written as

$$y(t) = A \sum_{i=1}^{\Omega} \exp\left[j\left(4\pi \frac{Bd_i(t)}{cT_d}t + 4\pi \frac{d_i(t)}{\lambda}\right)\right], \tag{5}$$

where λ denotes the wavelength of the chirp.

The complex IF signal $y(t)$ is digitized by an analog to digital converter (ADC). The dimension corresponding to N samples per chirp is called the fast time. The dimension corresponding to M different chirps is the slow time. Note

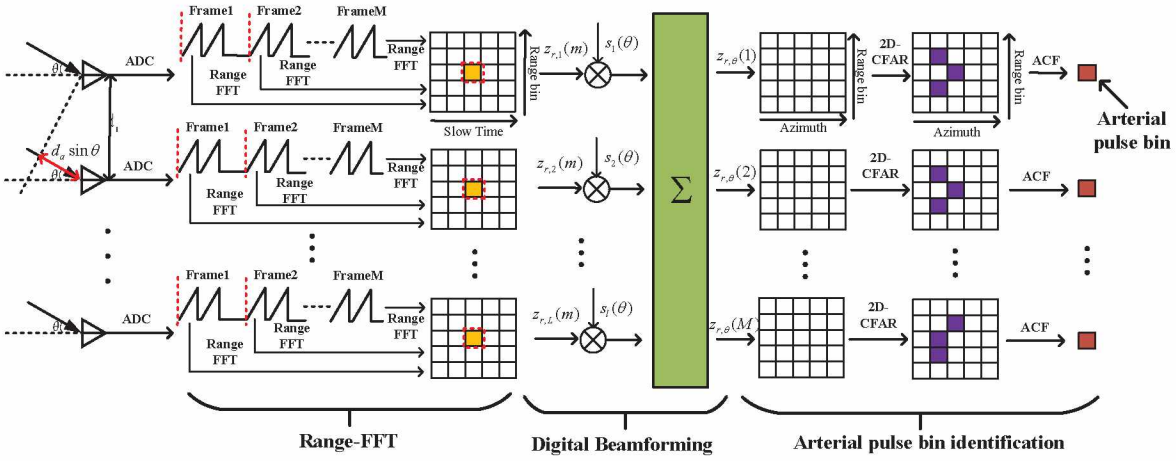

Fig. 3. The processing flow of the arterial pulse motion extraction

that the chirp duration is very small, and the distance change caused by arterial pulse motion is small (<2 mm) with low frequency (<3 Hz), therefore, there is no appreciable change in center frequency and phase during chirp time. Thus, the frame is used as the observation window for radar-based BP detection and only the first chirp in the frame is used for processing. mmRBP is with multiple transmit (TX) antennas and receive (RX) antennas, the chirps are transmitted in the time-division multiplexing (TDM) mode by multiple TX antennas. For an object at angle θ, an additional phase shift will occur due to the relative distance on adjacent antenna elements d_a, which can be expressed as $2\pi\frac{d_a \sin\theta}{\lambda}$. Therefore, for the lth antenna element, the digitized complex IF signal $y(n,m,l)$ for the nth ADC sample and mth chirp is written as

$$y(n,m,l) = A\sum_{i=1}^{\Omega}\exp\left[j\left(2\pi\underbrace{\frac{2Bd_i(nT_f)}{cT_d}}_{f_b}nT_f + \underbrace{4\pi\frac{d_i(nT_f+mT_s)}{\lambda} + 2\pi\frac{(l-1)d_a\sin\theta}{\lambda}}_{\phi_b}\right)\right], \tag{6}$$

where T_f and T_s are the time intervals, which correspond to the fast time and the slow time, respectively.

B. Arterial Pulse Motion Extraction

To achieve BP detection, mmRBP needs to extract mm-wave reflections containing arterial pulse motion, but it is not a trivial task because mm-wave reflections may be largely contaminated by the interference and background noise from the environment. Most of the existing approaches place a subject at zero-degree bearing to ensure sufficient signal quality and select the bin with the maximum energy in the range-azimuth plane to extract the phase signal. However, these proposals are far from practical as it is unrealistic to ensure that subjects are placed at zero-degree bearing every time in our daily environment. In addition, the subjects may not remain stationary all the time, which would lead to the location variation of the arterial pulse. As a result, the direction of the strongest reflection may not coincide with the arterial pulse motion but rather a different location on the arm.

In this section, we focus on the strongest reflection signals from arterial pulse motion, where the range-FFT and DBF are utilized to scan the space and the direction of the strongest arterial pulse motion is identified to extract phase signal. The processing flow is shown in Fig. 3.

1) Range-FFT and Digital Beamforming: As shown in (12), the mm-wave reflections corresponding to the reflecting object is a periodic signal in fast time, and the periodicity is related to the distance. To obtain the range information, FFT is performed over the fast time for the chirp (see Fig. 3), which is called the range-FFT and denoted as

$$z(r,m,l) = \sum_{n=0}^{N-1} y(n,m,l)\exp(-j2\pi rn/N\ ), \tag{7}$$

where $z(r,m,l)$ is the mm-wave reflections for the rth range bin, mth chirp and lth antenna element.

Furthermore, to obtain the azimuth information, DBF is conducted over all antenna elements for each range bin, as shown in Fig. 3. The mm-wave reflections $z_{r,\theta}(m)$ corresponding to range bin r and azimuth θ can be written as

$$z_{r,\theta}(m) = \mathbf{s}^H(\theta)\mathbf{z_{r,l}}(m) + \varepsilon(m), \tag{8}$$

where $\mathbf{z_{r,l}}(m) = [z_{r,1}(m), z_{r,2}(m), \ldots, z_{r,L}(m)]$ is the mm-wave reflection vector at range bin r overall all antenna elements. $\varepsilon(m)$ is the additive white Gaussian noise. $\mathbf{s}(\theta) = [s_1(\theta), s_2(\theta), \ldots, s_L(\theta)]^T$ is the steering vector towards angle θ. In mmRBP, Bartlett beamformer [46] is employed, and the coefficient of the lth antenna is

$$s_l(\theta) = \exp(-j2\pi\frac{(l-1)\times d_a\sin\theta}{\lambda}), \tag{9}$$

For each sample m in the slow time, there is a mm-wave reflection matrix $z(r,\theta)$ at different location bins with range bin r and azimuth θ. Therefore, mm-wave reflections are separated to bins of range and azimuth by range-FFT and DBF. Fig. 4(a) shows the amplitude of the mm-wave reflections at

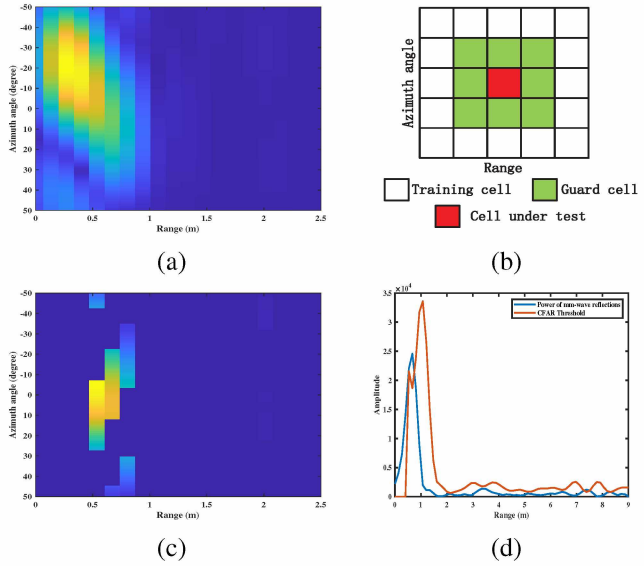

Fig. 4. Example of the reflecting object. (a) amplitude of mm-wave reflections in the range-azimuth plane, (b) 2D-CFAR window, (c) result of 2D-CFAR, and (d) the CFAR threshold and the amplitude of mm-wave reflections in range domain.

the range-azimuth plane. As mentioned above, the direction of the strongest reflection may not coincide with the arterial pulse motion but rather a different location on the arm. Thus, in the next section, we will try to identify the bin that has the strongest arterial pulse motion to extract the phase signal.

2) Arterial Pulse Bin Identification: In this section, mmRBP try to identify the bin that has the strongest arterial pulse motion in the range-azimuth plane. The challenge in achieving this is that, on the one hand, it does not know the exact appearance of the arterial pulse motion reflection and, on the other hand, this reflection may vary with the user, their wrist position and heart rate. To overcome this challenge, mmRBP exploits the fact that the arterial pulse signal is periodic, and leverages this periodicity to identify the best bin of obtaining the corresponding periodic signal. As shown in Fig. 3, the process of arterial pulse bin identification consists of two steps.

Firstly, we need to identify the bins with reflecting objects in the range-azimuth plane. In general, the energy of the bins without any reflecting objects is smaller than those with reflecting objects. However, it is difficult to find a threshold for all reflecting objects because the energy of reflecting objects is affected by many factors, such as the distance, and radar cross section, etc. In mmRBP, 2D-CFAR is employed to estimate the noise level, where the CFAR window (shown in Fig. 4(b)) is convolved with the mm-wave reflections of the range-azimuth bins. As a result, the range-azimuth bins with reflecting objects are those whose energy is above the noise level, as shown in Fig. 4(c). Fig. 4(d) shows the example of CFAR detection in the range domain.

Then, autocorrelation function (ACF) is performed over the candidate bins obtained by 2D-CFAR to evaluate the periodicity, as shown in Fig. 3. In specific, the bin with the highest peak for the first peak of the autocorrelation coefficient is selected, which corresponds to the arterial pulse bin with the strongest arterial pulse motion. Before ACF, the

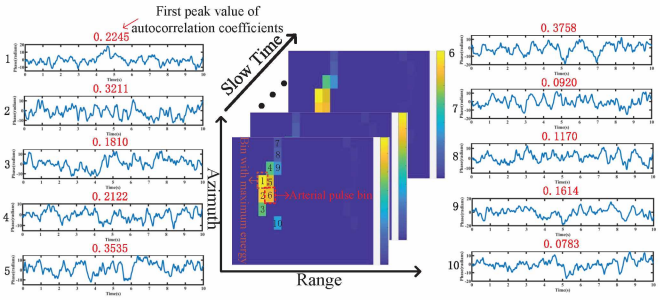

Fig. 5. The periodicity evaluation of phase signal.

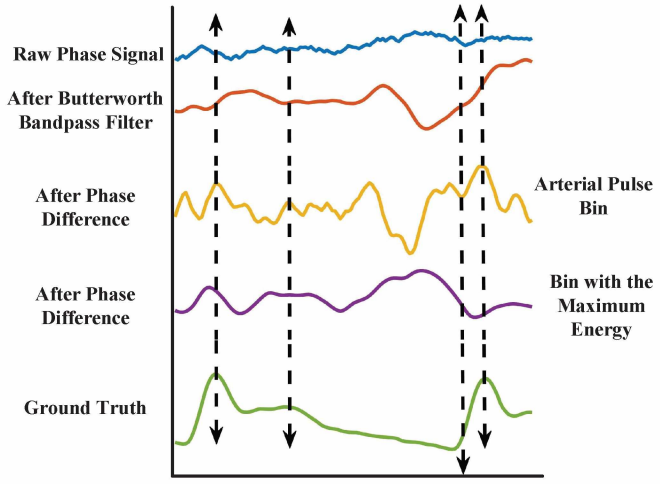

Fig. 6. Phase signal processing result at different stages of mmRBP's arterial pulse motion extraction, chronologically from top to bottom. After the Butterworth bandpass filter, the signal looks irrelevant to arterial pulse signal. After the phase difference, its trend starts showing some feature points. Besides, the extracted phase signal in arterial pulse bin has sharper peaks and troughs with strong arterial pulse motion compared with that in the bin with the maximum energy.

Butterworth bandpass filter is employed to remove baseline drift and high-frequency noise. In Fig. 5, the phase signals and their first peak values of the autocorrelation coefficients are presented. It is obvious that the periodicity of the bin with the maximum energy is not the best. Thus, instead of this bin, we select the bin with the highest peak for the first peak of the autocorrelation coefficients to extract phase signal containing strong arterial pulse motion. The phase difference is performed to convert the phased-based distance estimation to an acceleration by designing the filter as a second derivative, thus emphasizing the feature points related to arterial pulse signal.

Fig. 6 plots the signal waveforms at different stages of mmRBP's arterial pulse motion extraction, chronologically from top to bottom. The topmost plot shows the raw phase signal extracted from the candidate bins obtained by 2D-CFAR. The signal has the baseline drift due to the different sources of noise and interference. Thus, after applying a Butterworth bandpass filter, the baseline drift is removed as shown in the second plot from the top. However, the plot has no obvious variation and looks irrelevant to arterial pulse

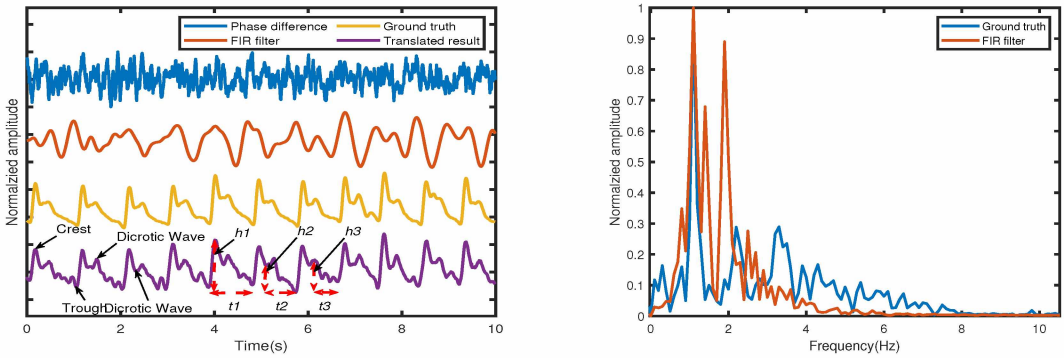

Fig. 7. The results of arterial pulse signal recovery.(a) arterial pulse signal. (b) the FFT of arterial pulse signal

signal. Fortunately, after the phase difference, it is apparent that there are some feature points related with arterial pulse signal as shown in the third plot from the top. Besides, we compare the phase difference signal between the bin with the maximum energy and arterial pulse bin. Notice that the signal of arterial pulse bin has sharper peaks and troughs with better SNR. However, notice that the phase difference signal still contains much noise and need to be processed in the next section.

C. Arterial Pulse Signal Translation

In practice, the phase difference signal extracted through the previous module is still contaminated by the noise, making it difficult to accurately estimate BP. Hence, phase difference signal needs to be translated to the fine-grained arterial pulse signal. In general, the finite impulse response (FIR) filter is utilized to perform such conversion, but in practice, it is challenging because mm-wave reflections and standard pulse wave signal acquisition methods, such as photoplethysmography (PPG), are fundamentally different acquisition mechanisms, with different front-ends, characteristics, and channel features. Due to these differences, it is difficult to derive a closed-form signal transformation from one modality to the other. As a result, FIR filter may filter out some useful detailed information in the arterial pulse signal (see the second plot from the top of Fig. 7(a)), such as dicrotic waves, dicrotic north, crest, trough and so on. As shown in Fig. 7(b), arterial pulse signal obtained by a FIR filter is coarse-grained and it can be used to estimate heart rate but not sufficient for BP estimation.

To tackle this challenge, CNN-based translation filter is designed to recover the fine-grained arterial pulse signal. Several CNN blocks are regarded as multiple FIR filters due to the same mathematical representation. The translation filter learns the filter's coefficients from phase difference signal and arterial pulse signal pairs. It enables us to recover fine-grained cardiovascular information from phase difference signal by the combination of various frequency components from mm-wave signals. As shown in Fig. 8, the input of this filter is the phase difference signal obtained from the output of the arterial pulse motion extraction module. The translation filter

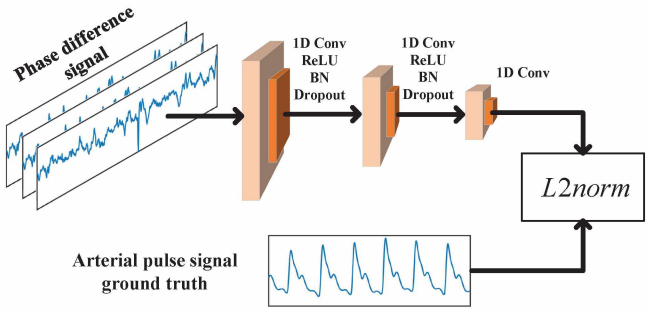

Fig. 8. The architecture of the CNN-based translation filter

consists of several CNN blocks, and each CNN block includes one-dimension convolution (1D Conv) with a rectified linear unit (ReLU) activation function, a batch normalization (BN) layer, and a dropout layer. ReLU functions are capable of extracting more complex features due to its nonlinearity. BN and dropout layers can prevent overfitting. Every CNN block has the same length but different channels. To update the coefficients of CNN blocks, the L2-norm is employed between the final output and the ground truth of arterial pulse signal (obtained from wearable sensor during training phase). Note that the translation filter does not require the wearable sensor during the test phase as it has already learned the translation function during training.

As observed from Fig. 7(a), the arterial pulse signal translation module enables it to recover the fine-grained arterial pulse signal from phase difference signal, and the cosine similarity is 0.98, which shows high consistency compared with the ground truth. Some researches have studied the relationship between BP and arterial pulse signal [20], [32], [39]. Scholars have studied diverse feature parameters, such as $h1$, $h2$, $h3$, $t1$, $t2$, $t3$ in Fig. 7(a). In the next section, we will attempt to establish the relationship between the BP and arterial pulse signal obtained from mm-wave reflections.

D. BP Estimation

There exists correlation between the arterial pulse signal and BP [43], [47]. Some existing researches attempt to achieve

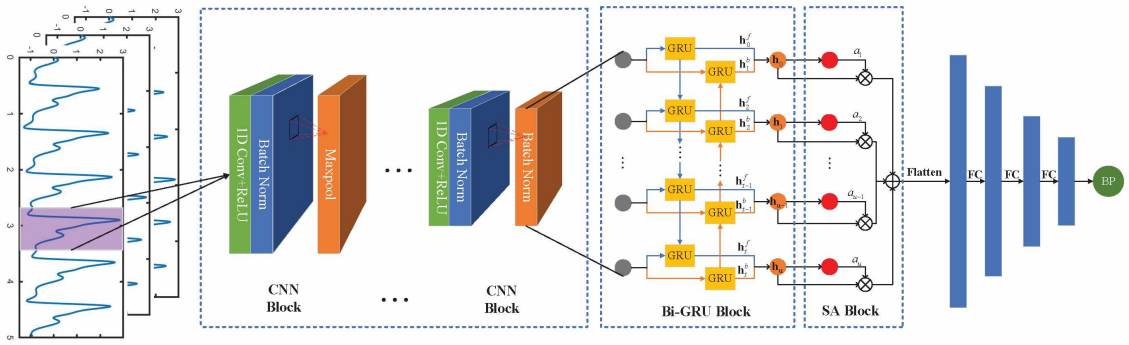

Fig. 9. The architecture of the source network

BP estimation from the arterial pulse signal based on PWV. PWV describes the speed that a BP pulse travels through the circulatory system. It is expressed as $PWV = \frac{L}{PTT}$, where L stands for the artery length that BP pulse passed through. According to Moeans and Korteweg [48], the PTT in the artery is calculated as

$$PTT = L/K \times \sqrt{\frac{\rho D}{Es}}, \tag{10}$$

where K is the Moens constant, s refers to the thickness of the blood vessel wall, E stands for the young's modulus of the artery wall's elasticity, D is the diameter of the inner wall of the artery, and ρ denotes the fluid density. Based on Hughes equation [48], the relationship between E and the difference pressure P between internal and external wall is denoted as

$$E = E_0 \exp(\xi P), \tag{11}$$

where ξ is the arterial material coefficient, and E_0 refers to the elastic modules of blood vessel when P is 0. Based on (10) and (11), the mean BP (MBP) [49], [50] can be obtained as

$$MBP = \frac{1}{3}SBP + \frac{2}{3}DBP = MBP_0 + \frac{2}{\gamma}\ln(\frac{b}{PTT}), \tag{12}$$

where MBP_0 and b are calibration factors, γ is a constant. By the Bramwell-Hill equation, the PWV can be expressed as $PWV = \sqrt{\frac{G \cdot \Delta P}{\rho \cdot \Delta G}}$, where G is the blood volume in the artery, ΔG is the blood volume change, and ΔP is the variance between SBP and DBP, which can be expressed as

$$\Delta P = SBP - DBP = \frac{\rho \Delta G}{G}\left(\frac{L}{PTT}\right)^2 = \frac{a}{PTT^2}, \tag{13}$$

where a is a calibration factor. Subsequently, SBP can be obtained as

$$SBP = DBP + \frac{a}{PTT^2}. \tag{14}$$

According to (12) and (14), DBP can be expressed as

$$DBP = MBP_0 + \frac{2}{\gamma}\ln(\frac{b}{PTT}) - \frac{1}{3}\frac{a}{PTT^2}. \tag{15}$$

Specifically, the obtained PTT, SBP, and DBP are substituted into (12), (14) and (15) to obtain a, b and MBP_0.

Once the calibration parameters have been calibrated, the SBP and DBP can be calculated by the PTT extracted from arterial pulse signal. However, PWV-based BP detection requires a calibration, making it less robust regarding generalization ability. Given the challenges encountered by the PWV, recent radar-based BP detection solutions have resorted to machine learning algorithm. However, such approaches are suffering from the demand for a large amount of training samples to train a model. In order to tackle this challenge, we design a DTL-based model to achieve accurate and reliable BP estimation with small amount of data, which mainly consists of the source network and the target network.

1) Source Network: The source network is trained using the BP public dataset as the feature extractor. It consists of several CNN blocks, a Bi-GRU block, a SA block and three FC layers, as shown in Fig. 9. The CNN blocks are employed to extract spatial features, followed by a Bi-GRU, which is designed to capture the temporal features. The output of the Bi-GRU hidden state vector is weighted by a SA block, and then the SBP, DBP and MAP results come out through three FC layers.

CNN is employed to extract spatial pattern features from arterial pulse signal, which consists of the 1D Conv with a ReLU, a BN layer, a max-pooling layer and a dropout layer. The last layer of each CNN block is set as a max-pooling layer to further extract effective features and reduce the dimension of features. The output of the last CNN block is flattened to one-dimension vector. Although CNN is capable of capturing spatial features, it is difficult to extract temporal information. To do that, we design a Bi-GRU block after the CNN block, which consists of a forward direction GRU and a backward direction GRU. The final output hidden vector h_t of the Bi-GRU can be written as

$$h_t = h_t^f \oplus h_t^b, \tag{16}$$

where h_t^f is the forward hidden vector and h_t^b is the backward hidden vector.

The sequential feature vectors from the Bi-GRU block may have different contributions for estimating BP, so a SA block is developed to automatically find the important feature vectors at each time step, as shown in Fig. 9. The important feature vectors will be assigned to larger weights, in which the importance score e_u is calculated through a score function

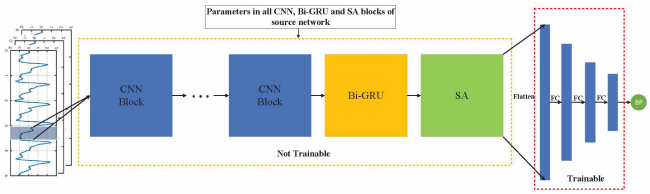

Fig. 10. The architecture of the target network

$score(\cdot)$ as follows:

$$e_u = score(\mathbf{W_e h_u} + g), \tag{17}$$

where $\mathbf{h_u}$ is the Bi-GRU hidden state vector at every time step $u \in [1, U]$, $\mathbf{W_e}$ is a trainable weight and g is a bias. The attention weight q_u is evaluated with softmax function, which is written as

$$q_u = soft\max(e_u) = \frac{\exp(e_u)}{\sum_u \exp(e_u)}. \tag{18}$$

The final output vector $\mathbf{v}$ is obtained by calculating the weighted sum of the attention weight vector and the corresponding hidden state vector, which is expressed as

$$\mathbf{v} = \sum_{u}^{U} q_u \mathbf{j_u}. \tag{19}$$

The output of the SA is flattened to one-dimension vector through a flatten layer. Then, the SBP, DBP and MAP come out through three FC layers.

2) Target Network: The target network is trained using the radar arterial pulse signal and termed as the BP estimation model. According to the previous analysis in the arterial pulse signal translation module, there is a high correlation between the radar arterial pulse signal and the ground truth of arterial pulse signal (shown in Fig. 7(a)). Therefore, the knowledge of the source network could be transferred to the target network based on DTL, when the well-trained source network with BP public dataset can decode all the representative information of BP.

Specifically, the well-trained source network is regarded as the feature extractor of the target network. The target network keeps part or all of the structure consistent with the source network, as shown in Fig. 10. For the training strategy with DTL, the parameters of CNN, Bi-GRU and SA blocks in the source network are transferred to the target network, and then be frozen. Only the parameters of three FC layers are trained using radar samples. However, for the training strategy without DTL, all layer parameters are obtained by training the whole target network using large amount of radar samples. As a result, DTL-based target network is capable of achieving accurate and reliable BP estimation with small-scale radar dataset.

III. Experimental Results and Analysis

In this section, the evaluation details of the proposed mmRBP is introduced, including experimental setup and setting, performance analysis, and the comparison with the state-of-art work.

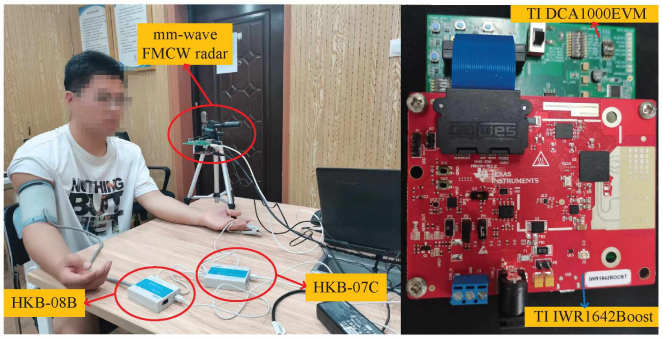

Fig. 11. The experimental scene used for human BP detection.

A. Experimental Setup and Setting

1) Experimental Setup: We conduct experiments using a commercial off-the-shelf Texas Instruments (TI) IWR1642Boost mm-wave radar with two TX antennas and four RX antennas. The device can achieve a theoretical azimuth resolution of 15°, and the field of view (FoV) is 120° in the horizontal plane and 30° in the vertical plane. Each frame is configured to have 2 chirps. The frame sampling rate is 100 Hz, the start frequency of a chirp is 77 GHz, the idle time of between chirps is 7 us, the duration time of a chirp is 60 us, the slope of a chirp is 64.985 MHz/s, the actual bandwidth of a chirp is 3.24925 GHz, the samples per chirp is 256, the ADC sample rate is 5.12 MHz. To collect raw mm-wave signals, TI DCA1000 board is used with IWR1642Boost mm-wave radar. The mm-wave signals are processed by a desktop PC.

2) Experimental Setting: All the experiments are carried out in an office, as shown in Fig. 11. The human subject is asked to sit on the chair and place his/her wrist on the desk (palms facing up). The FMCW mm-wave radar is set up at 15 cm above the human subject's wrist on the desk and emits the EM signals to the wrist and captures the echo signals. HKG-08B is used to collect the ground truth of BP simultaneously with the mmRBP during the experiment. Moreover, since the arterial pulse signal is used as the ground truth in the arterial pulse signal translation module, we record it synchronously with HKG-07C arterial pulse sensor, a wearable device on human subject's finger. 15 volunteers (10 males and 5 females, weighted between 45 and 93 kg, aged from 26 to 55 years old) are included in this study. The volunteers were free of known cardiac, respiratory, or any other diseases. They are university students, professions, and janitorial staffs. During data collection, volunteers are asked to remain stationary for 60 s. The data collection is performed on seven days, and 1500 samples are collected. To evaluate the performance of mmRBP, the mean error (ME), standard deviation (STD), Pearson's Correlation Coefficient (PCC) and root mean square error (RMSE) are utilized.

3) System Setting: In the arterial pulse signal translation module, we adopt three data augmentation approaches, including overlapping, stretching, noising, to train CNN-based translation filter. First, we use a sliding window function to divide the input signal into segments. The window consists of 1000 points and is shifted by 200 points to extract over-

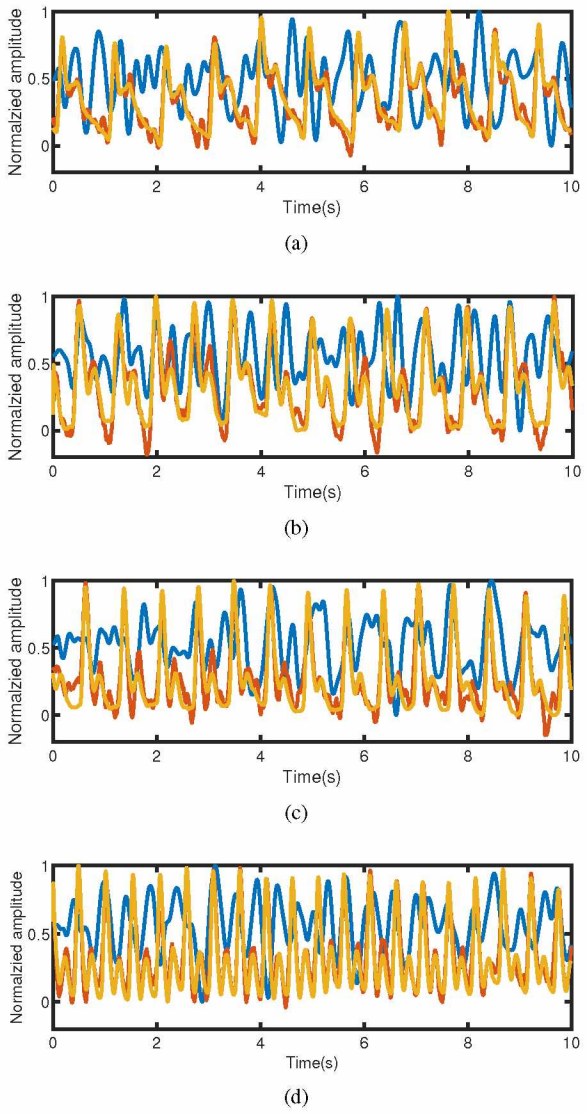

Fig. 12. Examples of arterial pulse signal recovery. The blue line indicates the FIR filter, the red line is mmRBP, and the yellow line is the ground truth.

lapping segments. Second, each signal segment is stretched or squeezed to represent a large number of heart rates (50-140 beats per minute(bpm), at 10 bpm intervals) using the cubic spline data interpolation. Third, each signal segment is replicated 10 times using different power of random noise. It generates 42000 samples for training, which can avoid overfitting. The Adam optimizer is used and the kernel size of 1D Conv is 101×1 with stride of 1. The batch size is set to 64, learning rate is set to 1e-5, and dropout rate is set to 0.2.

In the BP estimation module, the University of California Irvine BP (UCI-BP) dataset from UCI machine learning repository II is employed to train the source network. It consists of PPG and intra arterial blood pressure (IABP) signals from 12000 instances. The IABP signals are considered as the ground truth, from which SBP, DBP and MAP can be obtained: $SBP = \max(ABP)$, $DBP = \min(ABP)$ and $MAP = \frac{SBP+2DBP}{3}$. The recordings of the insufficient length (less than 3 minutes) are removed from the dataset. Moreover, some

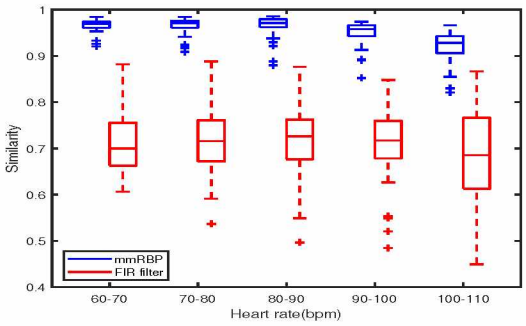

Fig. 13. Cosine similarity of arterial pulse sigal to ground truth under different heart rate ranges.

very high or low BP values (SBP≥180, SBP≤80, DBP≥130, and DBP≤60) have been filtered from the dataset to ensure high signal reliability. The PPG signal is processed by a second-order Butterworth bandpass filter to remove baseline wandering and power-line noise. A sliding window function is used to divide the PPG signal, and the window consists of 1000 points and is shifted by 200 points. Finally, the PPG signal is normalized and split into 80% for training and 20% for testing.

The kernel size of 1D Conv is 3×1 with stride of 1 and the fitting method is "same". The size of maximum pooling is 3 and the step size is 1. Bi-GRU has 64 hidden nodes for the the forward and backward layers, and there will be 128 features at each time step. Three FC layers contain 512 units, 256 units and 1 units, respectively. The Adam optimizer is used and the learning rate is set to 10^{-3}. The loss function is the mean squared error (MSE). During the source network training, the early stopping method is applied, which is with the patience of 10 in a maximum of 50 epochs. The batch size is set to 128. To avoid overfitting, L_2 regularize is applied. As for the target network, the obtained radar arterial pulse signal samples are split into 80% for training and 20% for testing.

B. Overall Performance

1) Arterial Pulse Signal Recovery: In this section, we present mmRBP's performance in recovering the arterial pulse signal from mm-wave reflections. The dataset is divided into a training set and testing set and the cross validation is employed to ensure that the training and testing are mutually exclusive. Specifically, for each subject, the model is trained on other subjects and evaluated on the untrained subject. In Fig. 12, we show the arterial pulse signals obtained by mmRBP for 5 individuals with different heart rates, and also compare mmRBP to a baseline approach that performs range-FFT, DBF, arterial pulse bin identification and FIR filter. It is obvious that the mmRBP outperforms the baseline approach.

To quantify the similarity between arterial pulse signal obtained by mmRBP and the ground truth, we calculate the cosine similarity under different heart rate ranges, as shown in Fig. 13, which represents how closely two variables move together. It shows that mmRBP enable it to learn representative transformations between the mm-wave reflections and the on body pulse sensor.

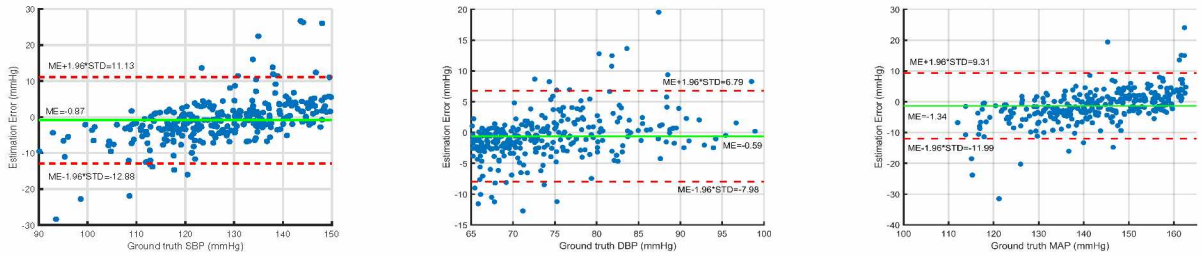

(a) (b) (c)

Fig. 14. Bland-Altman plots of SBP, DBP and MAP with mmRBP

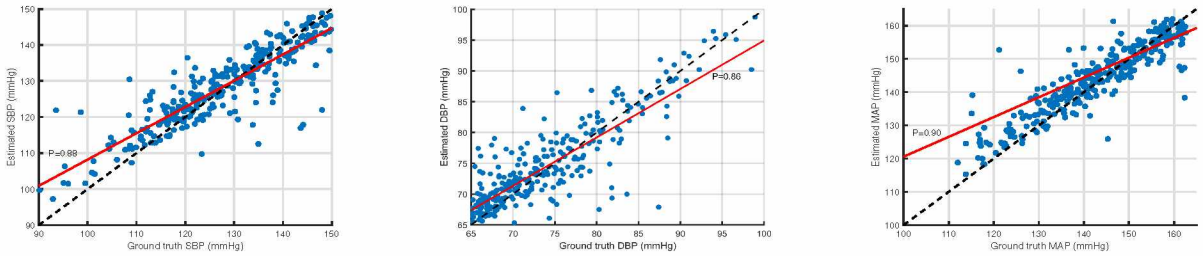

(a) (b) (c)

Fig. 15. Pearson correlation coefficients of SBP, DBP and MAP with mmRBP

2) BP Estimation: In this part, we evaluate the overall BP estimation performance of mmRBP. At first, we compare the error of mmRBP and the acceptable detection error defined by the AAMI standard, as shown in Table I. As observed from this table, the errors of mmRBP for both SBP and DBP are smaller than the error boundaries defined by the AAMI. To further verify detection performance, Table II compares the accuracy of mmRBP and requirement defined in the BHS standard. The results show that both SBP and DBP reach Grade A. The performance comparison between mmRBP and two BP measurement standards demonstrates that mmRBP achieves accurate and reliable BP estimation.

Then, we present the Bland-Altman plots of estimated SBP, DBP and MAP with mmRBP, as illustrated in Fig. 14. The green solid line denotes ME and the red dashed line denotes the limits of agreement (LoA), which is defined as ME$\pm$1.96$\times$STD. As observed from this figure, mmRBP achieves accurate and reliable BP estimation, in which more than 95 % data is within the area of LoA. Finally, to further verify the performance of mmRBP, we present the PCC of SBP, DBP and MAP estimated by mmRBP in Fig. 15. As illustrated in this figure, mmRBP achieves a high correlation (at least 0.86) for SBP, DBP and MAP. In other words, the estimated SBP, DBP and MAP have a high consistency with the corresponding ground truth, which verifies the feasibility and reliability of mmRBP.

TABLE I
PERFORMANCE COMPARISON OF MMRBP WITH AAMI STANDARD

Method	Type	ME (mmHg)	STD (mmHg)
AAMI	SBP	≤ 5	≤ 8
	DBP	≤ 5	≤ 8
mmRBP	SBP	0.87	6.12
	DBP	0.59	3.78

TABLE II
PERFORMANCE COMPARISON OF MMRBP WITH BHS STANDARD

Method	Type	≤ 5 (mmHg)	≤ 10 (mmHg)	≤ 15 (mmHg)
BHS	Grade A	60%	85%	95%
	Grade B	50%	75%	90%
	Grade C	40%	65%	85%
mmRBP	SBP	74.7%	91.3%	97.0%
	DBP	87.0%	96.3%	99.7%

C. Performance Comparison of Key Modules

In this section, we will compare the performance of mmRBP's modules. To do so, we evaluate the error of partial implementations of the overall system: (1) mmRBP's full architecture with its arterial pulse motion extraction, CNN-based translation filter and DTL-based BP estimation, (2) the phase signal of bin with the maximum energy is extracted and a FIR filter is applied to acquire arterial pulse signal (HP-FIR), (3) deep learning based BP estimation approach (DL).

Fig. 16(a) depicts the estimated error for mmRBP's full implementations and partial implementations (HP-FIR). It is

observed that HP-FIR achieves significantly higher errors than mmRBP's full implementation. As declared in Section II-B, the bin with the maximum energy may correspond to the static objects or other body parts with reflections caused by the weak arterial pulse motion. So the SNR of extracted arterial pulse motion may be low, and the FIR filter could not recover fine-grained arterial pulse signal from mm-wave reflections, which might lead to a large BP estimation error. Instead, in mmRBP, we apply range-FFT and DBF to divide the space into different range-azimuth bins and the arterial pulse bin is identified to extract mm-wave reflections containing the strongest arterial pulse motion. In addition, CNN-based translation filter is able to recover fine-grained arterial pulse signal from mm-wave reflections.

Fig. 16(b) depicts the estimated error of mmRBP's full implementations and partial implementations (DL). As observed from this figure, the BP estimation error of DL is higher than mmRBP. The main reason is that the small amount of data could not train a deep network model well, leading to a large BP estimation error. Differently, in mmRBP, we design a DTL-based model to achieve accurate and reliable BP estimation with small amount of radar samples.

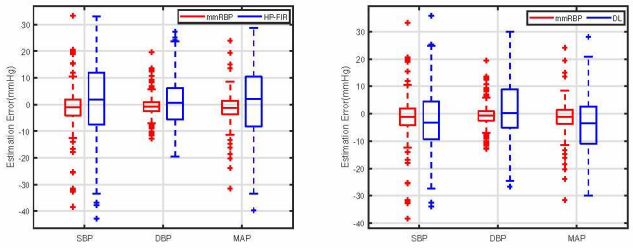

Fig. 16. Impact of proposed modules on BP detection accuracy. (a) mmRBP and HP-FIR. (b) mmRBP and DL.

D. Comparison Against State-of-the-art Work

In this section, we compare mmRBP with four baseline methods, including mmBP [20], NBPM [41], SMBP [45] and PhysioChair [38]. mmRBP, mmBP, NBPM and SMBP all require a single radar to achieve contactless BP detection. Differently, PhysioChair designed a dual-frequency radar system to achieve BP detection. The absolute error of BP detection is less than 5 mmHg. However, PhysioChair brings some challenges in the complexity of BP detection system because it needs a strict synchronization between the two radars.

As observed from Fig. 17, mmRBP outperforms other three baseline methods using a single radar with lower RMSE and STD. Random forest of NBPM and SVM of SMBP need to extract features from the arterial pulse signal. However, the signal obtained by radar is susceptible to noise, which brings a challenge in extracting effective pulse-related features. In mmBP, an encorder-decorder neural network is proposed to estimate BP, which needs to be trained by large amount of data, and it has a poor performance when there is small amount of data. In mmRBP, we apply the range-FFT and DBF to scan the space and identify the direction of the reflection coming from the strongest arterial pulse motion. Then, the CNN-based translation filter is designed to acquire fine-grained arterial pulse signal from mm-wave reflections. Finally, DTL-based BP estimation model is proposed, whose training requires only small amount of radar samples. Therefore, mmRBP achieves better performance for BP detection with mm-wave FMCW radar.

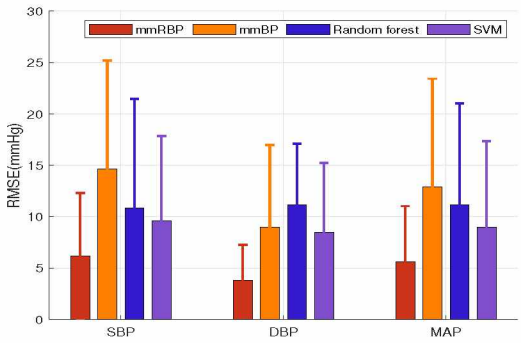

Fig. 17. Performance comparison between mmRBP and other baseline methods.

IV. Conclusion

In this paper, we develop mmRBP, a novel contactless and continuous BP detection system with FMCW mm-wave radar. It consists of three modules, including the arterial pulse motion extraction module to extract mm-wave reflections with high SNR by range-FFT, DBF and the arterial pulse bin identification, the arterial pulse signal translation module to acquire the fine-grained arterial pulse signal via CNN-based translation filter, and the BP estimation module to achieve continuous BP estimation with small-scale radar training samples by DTL. Extensive experimental results show that mmRBP satisfy both the BHS and AAMI BP measurement standards, and outperforms other approaches with small amount of data. In the future, there are still some challenges that need to be addressed, including overcoming the interference of random body movements, multi-person BP detection, and long-distance BP detection.

References

[1] Y. Chen, D. Zhang, H. R. Karimi, C. Deng, and W. Yin, "A new deep learning framework based on blood pressure range constraint for continuous cuffless bp estimation," *Neural Networks*, vol. 152, pp. 181–190, 2022.

[2] D. Barvik, M. Cerny, M. Penhaker, and N. Noury, "Noninvasive continuous blood pressure estimation from pulse transit time: A review of the calibration models," *IEEE Reviews in Biomedical Engineering*, vol. 15, pp. 138–151, 2021.

[3] M. Yavarimanesh, R. C. Block, K. Natarajan, L. K. Mestha, O. T. Inan, J.-O. Hahn, and R. Mukkamala, "Assessment of calibration models for cuff-less blood pressure measurement after one year of aging," *IEEE Transactions on Biomedical Engineering*, vol. 69, no. 6, pp. 2087–2093, 2021.

[4] N. Aguirre, E. Grall-Maës, L. J. Cymberknop, and R. L. Armentano, "Blood pressure morphology assessment from photoplethysmogram and demographic information using deep learning with attention mechanism," *Sensors*, vol. 21, no. 6, p. 2167, 2021.

[5] T. W. Gress, F. J. Nieto, E. Shahar, M. R. Wofford, and F. L. Brancati, "Hypertension and antihypertensive therapy as risk factors for type 2 diabetes mellitus," *New England Journal of Medicine*, vol. 342, no. 13, pp. 905–912, 2000.

[6] A. Al-Makki, D. DiPette, P. K. Whelton, M. H. Murad, R. A. Mustafa, S. Acharya, H. M. Beheiry, B. Champagne, K. Connell, M. T. Cooney *et al.*, "Hypertension pharmacological treatment in adults: a world health organization guideline executive summary," *Hypertension*, vol. 79, no. 1, pp. 293–301, 2022.

[7] J. Liu, B. Yan, S.-C. Chen, Y.-T. Zhang, C. Sodini, and N. Zhao, "Non-invasive capillary blood pressure measurement enabling early detection and classification of venous congestion," *IEEE Journal of Biomedical and Health Informatics*, vol. 25, no. 8, pp. 2877–2886, 2021.

[8] D. Nachman, Y. Gepner, N. Goldstein, E. Kabakov, A. B. Ishay, R. Littman, Y. Azmon, E. Jaffe, and A. Eisenkraft, "Comparing blood pressure measurements between a photoplethysmography-based and a standard cuff-based manometry device," *Scientific reports*, vol. 10, no. 1, p. 16116, 2020.

[9] L. Li, Y. Li, L. Yang, F. Fang, Z. Yan, and Q. Sun, "Continuous and accurate blood pressure monitoring based on wearable optical fiber wristband," *IEEE Sensors Journal*, vol. 21, no. 3, pp. 3049–3057, 2020.

[10] A. Chandrasekhar, M. Yavarimanesh, K. Natarajan, J.-O. Hahn, and R. Mukkamala, "Ppg sensor contact pressure should be taken into account for cuff-less blood pressure measurement," *IEEE Transactions on Biomedical Engineering*, vol. 67, no. 11, pp. 3134–3140, 2020.

[11] S. Shin, A. S. Mousavi, S. Lyle, E. Jang, P. Yousefian, R. Mukkamala, D.-G. Jang, U. K. Kwon, Y. H. Kim, and J.-O. Hahn, "Posture-dependent variability in wrist ballistocardiogram-photoplethysmogram pulse transit time: implication to cuff-less blood pressure tracking," *IEEE Transactions on Biomedical Engineering*, vol. 69, no. 1, pp. 347–355, 2021.

[12] B.-J. Wu, B.-F. Wu, and C.-P. Hsu, "Camera-based blood pressure estimation via windkessel model and waveform features," *IEEE Transactions on Instrumentation and Measurement*, vol. 72, pp. 1–13, 2023.

[13] Y. Zhou, H. Ni, Q. Zhang, and Q. Wu, "The noninvasive blood pressure measurement based on facial images processing," *IEEE Sensors Journal*, vol. 19, no. 22, pp. 10 624–10 634, 2019.

[14] C. Zhang, E. Jovanov, H. Liao, Y.-T. Zhang, B. Lo, Y. Zhang, and C. Guan, "Video based cocktail causal container for blood pressure classification and blood glucose prediction," *IEEE Journal of Biomedical and Health Informatics*, vol. 27, no. 2, pp. 1118–1128, 2023.

[15] D. Djeldjli, F. Bousefsaf, C. Maaoui, F. Bereksi-Reguig, and A. Pruski, "Remote estimation of pulse wave features related to arterial stiffness and blood pressure using a camera," *Biomedical Signal Processing and Control*, vol. 64, p. 102242, 2021.

[16] H. L. Seldon, B. T. Lau, and Y. L. Ong, "New ways to estimate blood pressure, heartrate variability and spo2 via smartphone camera–proof of concept," in *MobiQuitous 2020-17th EAI International Conference on Mobile and Ubiquitous Systems: Computing, Networking and Services*, 2020, pp. 451–457.

[17] Z. Shi, T. Gu, Y. Zhang, and X. Zhang, "mmbp: Contact-free millimetre-wave radar based approach to blood pressure measurement," in *Proceedings of the 20th ACM Conference on Embedded Networked Sensor Systems*, 2022, pp. 667–681.

[18] J. Shi and K. Lee, "Systolic blood pressure measurement algorithm with mmwave radar sensor," *KSII Transactions on Internet and Information Systems (TIIS)*, vol. 16, no. 4, pp. 1209–1223, 2022.

[19] B. Jana, K. Oswal, S. Mitra, G. Saha, and S. Banerjee, "Windkessel model-based cuffless blood pressure estimation using continuous wave doppler ultrasound system," *IEEE Sensors Journal*, vol. 20, no. 17, pp. 9989–9999, 2020.

[20] Y. Ran, D. Zhang, J. Chen, Y. Hu, and Y. Chen, "Contactless blood pressure monitoring with mmwave radar," in *GLOBECOM 2022-2022 IEEE Global Communications Conference*. IEEE, 2022, pp. 541–546.

[21] S. Ishizaka, K. Yamamoto, and T. Ohtsuki, "Non-contact blood pressure measurement using doppler radar based on waveform analysis by lstm," in *ICC 2021-IEEE International Conference on Communications*. IEEE, 2021, pp. 1–6.

[22] R. Kawasaki and A. Kajiwara, "Continuous blood pressure monitoring with mmw radar sensor," *IEICE Communications Express*, vol. 10, no. 12, pp. 997–1002, 2021.

[23] F. Adib, H. Mao, Z. Kabelac, D. Katabi, and R. C. Miller, "Smart homes that monitor breathing and heart rate," in *Proceedings of the 33rd annual ACM conference on human factors in computing systems*, 2015, pp. 837–846.

[24] L. Liu, J. Zhang, Y. Qu, S. Zhang, and W. Xiao, "mmrh: Noncontact vital sign detection with an fmcw mm-wave radar," *IEEE Sensors Journal*, vol. 23, no. 8, pp. 8856–8866, 2023.

[25] L. Liu, S. Zhang, and W. Xiao, "Noncontact vital signs detection using joint wavelet analysis and autocorrelation computation," *Chinese Journal of Engineering*, vol. 43, no. 9, pp. 1206–1214, 2021.

[26] J. Chen, D. Zhang, Z. Wu, F. Zhou, Q. Sun, and Y. Chen, "Contactless electrocardiogram monitoring with millimeter wave radar," *IEEE Transactions on Mobile Computing*, 2022, doi:10.1109/TMC.2022.321472.

[27] U. Ha, S. Assana, and F. Adib, "Contactless seismocardiography via deep learning radars," in *Proceedings of the 26th annual international conference on mobile computing and networking*, 2020, pp. 1–14.

[28] C. Will, K. Shi, S. Schellenberger, T. Steigleder, F. Michler, J. Fuchs, R. Weigel, C. Ostgathe, and A. Koelpin, "Radar-based heart sound detection," *Scientific reports*, vol. 8, no. 1, pp. 1–14, 2018.

[29] H. Zhao, X. Gu, H. Hong, Y. Li, X. Zhu, and C. Li, "Non-contact beat-to-beat blood pressure measurement using continuous wave doppler radar," in *2018 IEEE/MTT-S International Microwave Symposium-IMS*. IEEE, 2018, pp. 1413–1415.

[30] R. Kawasaki and A. Kajiwara, "Continuous blood pressure estimation using millimeter wave radar," in *2022 IEEE Radio and Wireless Symposium (RWS)*. IEEE, 2022, pp. 135–137.

[31] C. Liao, O. Shay, E. Gomes, and N. Bikhchandani, "Noninvasive continuous blood pressure measurement with wearable millimeter wave device," in *2021 IEEE 17th International Conference on Wearable and Implantable Body Sensor Networks (BSN)*. IEEE, 2021, pp. 1–5.

[32] Y. Ma, J. Choi, A. Hourlier-Fargette, Y. Xue, H. U. Chung, J. Y. Lee, X. Wang, Z. Xie, D. Kang, H. Wang *et al.*, "Relation between blood pressure and pulse wave velocity for human arteries," *Proceedings of the National Academy of Sciences*, vol. 115, no. 44, pp. 11 144–11 149, 2018.

[33] R. Wang, W. Jia, Z.-H. Mao, R. J. Sclabassi, and M. Sun, "Cuff-free blood pressure estimation using pulse transit time and heart rate," in *2014 12th international conference on signal processing (ICSP)*. IEEE, 2014, pp. 115–118.

[34] M. Kuwahara, E. Yavari, and O. Boric-Lubecke, "Non-invasive, continuous, pulse pressure monitoring method," in *2019 41st annual international conference of the IEEE Engineering in Medicine and Biology Society (EMBC)*. IEEE, 2019, pp. 6574–6577.

[35] D. Buxi, J.-M. Redouté, and M. R. Yuce, "Blood pressure estimation using pulse transit time from bioimpedance and continuous wave radar," *IEEE Transactions on Biomedical Engineering*, vol. 64, no. 4, pp. 917–927, 2016.

[36] M. Pour Ebrahim, F. Heydari, T. Wu, K. Walker, K. Joe, J.-M. Redoute, and M. R. Yuce, "Blood pressure estimation using on-body continuous wave radar and photoplethysmogram in various posture and exercise conditions," *Scientific Reports*, vol. 9, no. 1, p. 16346, 2019.

[37] T. Lauteslager, M. Tommer, T. S. Lande, and T. G. Constandinou, "Coherent uwb radar-on-chip for in-body measurement of cardiovascular dynamics," *IEEE transactions on biomedical circuits and systems*, vol. 13, no. 5, pp. 814–824, 2019.

[38] L. Wen, Y. Gao, C. Gu, and J. Mao, "Physiochair: A dual-frequency radar system for noninvasive and continuous detection of physiological signatures," *IEEE Sensors Journal*, vol. 22, no. 8, pp. 8224–8233, 2022.

[39] L. Singh, S. You, B. J. Jeong, C. Koo, and Y. Kim, "Remote estimation of blood pressure using millimeter-wave frequency-modulated continuous-wave radar," *Sensors*, vol. 23, no. 14, p. 6517, 2023.

[40] X. Jiang, J. Zhang, W. Mu, K. Wang, L. Li, and L. Zhang, "Trccbp: Transformer network for radar-based contactless continuous blood pressure monitoring," *Sensors*, vol. 23, no. 24, p. 9680, 2023.

[41] H. Shi, J. Pan, Z. Zheng, B. Wang, C. Shen, and Y. Guo, "Radar-based blood pressure estimation using multiple features," in *2022 IEEE MTT-S International Microwave Biomedical Conference (IMBioC)*. IEEE, 2022, pp. 183–185.

[42] F. Geng, Z. Bai, H. Zhang, Y. Yao, C. Liu, P. Wang, X. Chen, L. Du, X. Li, B. Han *et al.*, "Contactless and continuous blood pressure measurement according to captt obtained from millimeter wave radar," *Measurement*, vol. 218, p. 113151, 2023.

[43] W. Wang, P. Mohseni, K. L. Kilgore, and L. Najafizadeh, "Cuff-less blood pressure estimation from photoplethysmography via visibility graph and transfer learning," *IEEE Journal of Biomedical and Health Informatics*, vol. 26, no. 5, pp. 2075–2085, 2021.

[44] D.-K. Kim, Y.-T. Kim, H. Kim, and D.-J. Kim, "Deepcnap: A deep learning approach for continuous noninvasive arterial blood pressure monitoring using photoplethysmography," *IEEE Journal of Biomedical and Health Informatics*, vol. 26, no. 8, pp. 3697–3707, 2022.

[45] M. Jung, M. Caris, and S. Stanko, "Non-contact blood pressure estimation using a 300 ghz continuous wave radar and machine learning models," in *2021 IEEE International Symposium on Medical Measurements and Applications (MeMeA)*, 2021, pp. 1–6.

[46] C. S. Marino and P. M. Chau, "High-resolution doa estimation from synthetic aperture beamforming," in *2005 IEEE Antennas and Propagation Society International Symposium*, vol. 3. IEEE, 2005, pp. 279–282.

[47] Y. Lu, C. Wang, and M. Q.-H. Meng, "Video-based contactless blood pressure estimation: A review," in *2020 IEEE International Conference on Real-time Computing and Robotics (RCAR)*, 2020, pp. 62–67.

[48] X.-R. Ding, N. Zhao, G.-Z. Yang, R. I. Pettigrew, B. Lo, F. Miao, Y. Li, J. Liu, and Y.-T. Zhang, "Continuous blood pressure measurement from invasive to unobtrusive: Celebration of 200th birth anniversary of carl ludwig," *IEEE journal of biomedical and health informatics*, vol. 20, no. 6, pp. 1455–1465, 2016.

[49] C. Poon and Y. Zhang, "Cuff-less and noninvasive measurements of arterial blood pressure by pulse transit time," in *2005 IEEE engineering in medicine and biology 27th annual conference*. IEEE, 2006, pp. 5877–5880.

[50] Y.-L. Zheng, B. P. Yan, Y.-T. Zhang, and C. C. Poon, "An armband wearable device for overnight and cuff-less blood pressure measurement," *IEEE transactions on biomedical engineering*, vol. 61, no. 7, pp. 2179–2186, 2014.